

# Area Equivalent WKB Compact Modeling Approach for Tunneling Probability in Hetero-Junction TFETs Including Ambipolar Behavior

Fabian Horst, Atieh Farokhnejad, Ghader Darbandy, Benjamín Iníiguez, and Alexander Kloes

**Abstract**—This paper introduces an innovative modeling approach for calculating the band-to-band (B2B) tunneling probability in tunnel-field effect transistors (TFETs). The field of application is the usage in TFET compact models.

Looking at a tunneling process in TFETs, carriers try to tunnel through an energy barrier which is defined by the device band diagram. The tunneling energy barrier is approximated by an approach which assumes an area equivalent (AE) triangular shaped energy profile. The simplified energy triangle is suitable to be used in the Wentzel-Kramers-Brillouin (WKB) approximation. Referring to the area instead of the electric field at individual points is shown to be a more robust approach in terms of numerical stability. The derived AE approach is implemented in an existing compact model for double-gate (DG) TFETs.

In order to verify and show the numerical stability of this approach, modeling results are compared to TCAD Sentaurus simulation data for various sets of device parameters, whereby the simulations include both ON- and AMBIPOLAR-state of the TFET. In addition to the various device dimensions, the source material is also changed to demonstrate the feasibility of simulating hetero-junctions. Comparing the modeling approach with TCAD data shows a good match. Apart the limitations demonstrated and discussed in this paper, the main advantage of the AE approach is the simplicity and a better fit to TCAD data in comparison to the quasi-2D WKB approach.

**Index Terms**—TFET, tunneling probability, WKB approximation, hetero-junction, compact modeling, closed-form, double-gate (DG), ambipolarity

## I. INTRODUCTION

The conventional CMOS technology put forth the most advanced and improved semiconductor devices of the present days. The ongoing scaling of the MOSFETs down to the nanoscale domain for high speed applications, low package densities and ultra-low power consumption has revealed the short-channel effects as well as quantum mechanical effects [1], [2]. The carrier transport in MOSFETs, which is based on the thermionic emission, limits the subthreshold slope to  $S_{th} = 60 \text{ mV/dec}$ .

Turning the quantum mechanical effect of carrier tunneling through an energy barrier into an advantage has opened the possibility to introduce the TFET technology. Since the carrier

This project was supported by the German Federal Ministry of Education and Research under contract No. FKZ 13FH010IX5 and the Spanish Ministry of Economy and Competitiveness through project GREENSENSE (TEC2015-67883- R).

Fabian Horst, Anita Farokhnejad, Ghader Darbandy and Alexander Kloes are with the NanoP, TH Mittelhessen University of Applied Sciences, 35390 Giessen, Germany (e-mail: fabian.horst@ei.thm.de).

Benjamín Iníiguez is with the Universitat Rovira i Virgili, 43007 Tarragona, Spain (e-mail: benjamin.iniguez@urv.cat).

transport in TFETs is based on the B2B tunneling mechanism, achieving a subthreshold slope of  $S_{th} < 60 \text{ mV/dec}$  at room temperature and a small leakage current are feasible. In addition, TFETs grant a supply voltage  $V_{dd}$  reduction without increasing the leakage current [3]–[5].

Regarding TFETs the quantum mechanical transmission coefficient plays an important role in the calculation of the tunneling probability and consequently in the calculation of the B2B tunneling current. In general, the transmission coefficient is obtained by solving Schrödinger wave equation [6].

In fact, there is no closed-form solution for Schrödinger equation in which an arbitrary shaped energy barrier, except rectangular energy barrier, is considered. In WKB approximation which is the most commonly approach to calculate the tunneling probability  $T_{tun}$ , a triangular barrier shape is considered for any arbitrary energy barrier [6], [7].

With respect to the aforementioned difficulties in calculating the tunneling probability, this work introduces an innovative way to characterize the triangular energy barrier applied in the WKB approximation. The triangle is determined with the help of an AE approach. The AE approach is suitable for a numerically robust implementation in compact models of homo- and hetero-junction TFETs by taking into account the ON-state as well as the AMBIPOLAR behavior of the device.

For verification purpose, the AE approach is implemented in an existing compact model for DG TFETs introduced in [8]. Thus, the compact model is reviewed in this work to introduce the closed-form expressions of the electrostatics, band diagram, tunneling length and the B2B tunneling current for both ON- and AMBIPOLAR-state of the device.

By implementing the AE WKB approach in the existing compact model, TCAD Sentaurus simulation data of DG TFETs are used to designate the validity and the numerical robustness of the approach. Therefore, TCAD simulations are performed for different source materials, structural parameters and bias conditions. Additionally, the AE approach is compared to an existing quasi-2D WKB approach presented in [9].

## II. COMPACT DC TFET MODEL

For preliminary consideration, the compact DC TFET model presented in [8], [10] is reviewed and the AMBIPOLAR-state modeling is explained in detail in this section. The compact model is used to derive the AE WKB approach in section III.

The TFET model deals with a compact expression for the electrostatics and the device band diagram, which charac-



$$\varphi_x^{\text{ch,d}}(x, y) = \frac{k_d(y)}{x - l_d(y)} + m_d(y), \quad (8)$$

whereby the parameters  $a_d(y)$ ,  $b_d(y)$ ,  $c_d(y)$ ,  $k_d(y)$ ,  $l_d(y)$  and  $m_d(y)$  are calculated in dependency of  $y$  by applying four points  $P_1^d \dots P_4^{s/d}$  (see Fig. 2) and solving a linear equation system for the drain and channel region, respectively. The points are calculated by using the 2D analytical closed-form potential solution. In addition, Eq. (3) is applied in order to model the  $y$ -dependency of the potential.

The band diagram in the channel considering hetero-junctions is obtained by using Eq. (8):

$$E_{c/v}^{\text{ch,d}}(x, y) = -q \cdot \varphi_x^{\text{ch,d}}(x, y) + \chi_s - \chi_{\text{ch}} \pm \frac{E_g^{\text{ch}}}{2}, \quad (9)$$

where the band diagram in drain is given by implementing Eq. (7):

$$E_{c/v}^{\text{d}}(x, y) = -q \cdot \varphi_x^{\text{d}}(x, y) + \chi_s - \chi_d \pm \frac{E_g^{\text{d}}}{2}, \quad (10)$$

with the band gap  $E_g^{\text{d}}$  and the electron affinity  $\chi_d$  in drain region to take into account hetero-junctions. Due to the high drain doping concentration the model of Del Alamo [14] is applied to capture bgn effects.

### B. Tunneling Length

Using the compact equations of the band diagram, closed-form expressions for the tunneling length  $l_{\text{tun}}$  in the ON- and AMBIPOLAR-state, can be found. The tunneling length is derived along the  $x$ -axis for an arbitrary  $y$ -position.

A compact equation for the ON-state, located at the source-to-channel junction, is achieved with the help of the analytical expressions (5) and (6) for the band diagram. The horizontal distance between  $E_c^{\text{ch,s}}$  at a chosen  $x$ -value  $x_t^s$  and  $E_v^s$  at the same energy is defined by (see Fig. 3(a)):

$$l_{\text{tun}}^s(x_t^s, y) = x_t^s + \frac{b_s}{2 \cdot a_s} - \sqrt{\frac{1}{a_s} \cdot \left( \frac{k_s}{x_t^s - l_s} + m_s + K_1^s \right)}, \quad (11)$$

whereby  $x_t^s \in \{0 \dots l_{\text{ch}}/2\}$  and  $K_1^s$  is given by:

$$K_1^s = \frac{b_s^2}{4 \cdot a_s} - c_s + \frac{\chi_{\text{ch}} - \chi_s}{q} - \frac{E_g^{\text{ch}} + E_g^s}{2 \cdot q}. \quad (12)$$

The tunneling length in the AMBIPOLAR-state, characterized by the drain-to-channel junction, is obtained by using the analytical band diagram Eqs. (9) and (10). The horizontal distance between the channel valence band  $E_v^{\text{ch,d}}$  and the conduction band in drain  $E_c^{\text{d}}$  at the same energy, as it can be seen in Fig. 3(b), is given by:

$$l_{\text{tun}}^{\text{d}}(x_t^{\text{d}}, y) = -x_t^{\text{d}} - \frac{b_d}{2 \cdot a_d} - \sqrt{\frac{1}{a_d} \cdot \left( \frac{k_d}{x_t^{\text{d}} - l_d} + m_d + K_1^{\text{d}} \right)}, \quad (13)$$

with  $x_t^{\text{d}} \in \{l_{\text{ch}}/2 \dots l_{\text{ch}}\}$  and using:

$$K_1^{\text{d}} = \frac{b_d^2}{4 \cdot a_d} - c_d + \frac{\chi_{\text{ch}} - \chi_d}{q} + \frac{E_g^{\text{ch}} + E_g^{\text{d}}}{2 \cdot q}. \quad (14)$$

For simplification the parameters  $a_{s/d}(y)$ ,  $b_{s/d}(y) \dots m_{s/d}$ , that characterize the potential (see section II-A) are written

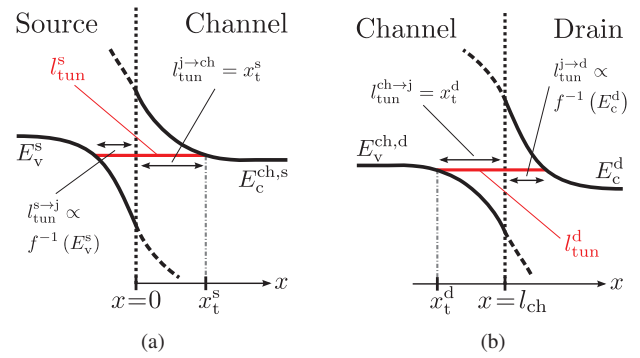


Figure 3. Schematic band diagram illustrating the tunneling length at (a) the source-to-channel junction which characterizes the ON-state and (b) the drain-to-channel junction describing the AMBIPOLAR-state of the device. The tunneling length  $l_{\text{tun}}^{s/d}$  consists of two parts, the first one is obtained by the inverse function of the valence/conduction band  $E_{v/c}^{s/d}$  in source/drain. The second one is defined by the chosen  $x$ -position  $x_t^{s/d}$  itself.

without their  $y$ -dependency in Eq. (11)–(14) and in all following equations. However, these parameters still depend on the chosen  $y$ -position.

### C. Tunneling Generation Rate

The tunneling generation rate (TGR) characterizes the number of carriers generated per second and per volume in the conduction band (ON-state) or valence band (AMBIPOLAR-state) of the channel by tunneling. The TGR is specified using the current density of the Tsu-Esaki formula [7], [15], which was originally proposed by Duke [16]. In this formula the integration over energy is substituted by an integration over  $x$  as:

$$J(y) = q \cdot \int_x TGR^{s/d}(x, y) dx \quad (15)$$

$$= q \cdot \int_x \frac{4 \cdot \pi \cdot m_{s/d}^*}{h^3} \cdot T_{\text{tun}}^{s/d}(\mathcal{E}(x, y)) \cdot N^{s/d}(\mathcal{E}(x, y)) \cdot q |\vec{E}| dx,$$

with the effective carrier mass  $m_{s/d}^*$ , elementary charge  $q$ , Planck's constant  $h$ , the considered energy  $\mathcal{E}$ , tunneling probability  $T_{\text{tun}}^{s/d}$  and electric field  $\vec{E}$ . The electric field is calculated by using the analytical approximation of the potential.

The effective mass  $m_s^*$  is the electron mass in source used to calculate the TGR in the ON-state, where  $m_d^*$  is the hole mass in drain applied in the TGR calculations for the AMBIPOLAR-state. The supply function for the ON-state  $N^s$  is defined by [7]:

$$N^s(\mathcal{E}(x, y)) = k \cdot T \cdot \ln \left( \frac{1 + \exp\left(-\frac{\mathcal{E}(x, y) - E_t^s}{k \cdot T}\right)}{1 + \exp\left(-\frac{\mathcal{E}(x, y) - E_t^{\text{d}}}{k \cdot T}\right)} \right) \quad (16)$$

and for the AMBIPOLAR-state follows:

$$N^{\text{d}}(\mathcal{E}(x, y)) = k \cdot T \cdot \ln \left( \frac{1 + \exp\left(-\frac{E_t^{\text{d}} - \mathcal{E}(x, y)}{k \cdot T}\right)}{1 + \exp\left(-\frac{E_t^s - \mathcal{E}(x, y)}{k \cdot T}\right)} \right), \quad (17)$$

using the Boltzmann constant  $k$ , temperature  $T$ , the Fermi level in source and drain region  $E_t^s$  and  $E_t^{\text{d}}$ , respectively.

The TGR allows to verify the modeling approach (see section III) with the help of TCAD Sentaurus simulation data, since the tunneling probability itself cannot be extracted from the simulation results.

For the compact modeling purpose the TGR needs to be expressed by an analytical function which is integrable in a closed-form. In [8] this has been done considering a Gaussian distribution as it can be seen in the TCAD data in Fig. 10:

$$TGR_{\text{comp}}^{s/d}(x, y) = TGR_{\text{max}}^{s/d}(y) \cdot \exp\left(-\frac{(x - x_{\text{max}}^{s/d}(y))^2}{\sigma^2}\right), \quad (18)$$

with the  $x$ -position of the maximum TGR value  $x_{\text{max}}^{s/d}$  obtained by first derivative of  $l_{\text{tun}}^{s/d}$ , indicating the position with the minimum tunneling length, and the maximum value of the TGR  $TGR_{\text{max}}^{s/d}$  calculated by means of Eq. (15) using  $x_{\text{max}}^{s/d}$ . The variance  $\sigma^2$  of the TGR is used as an adjustable parameter.

#### D. Tunneling Current Density

The second last step of the B2B tunneling current calculation is to find a compact expression for the current density  $J_{\text{comp}}^{s/d}$  along the  $y$ -axis. Using Eqs. (15) and (18) provides the possibility to characterize the tunneling current density at any  $y$ -position.

By picking the current density at the channel surface  $J_{\text{sur}}^{s/d}(y_{\text{sur}} = 0 \text{ nm})$  and center  $J_{\text{cen}}^{s/d}(y_{\text{cen}} = t_{\text{ch}}/2)$ , the compact current density is expressed by a Gaussian distribution [8]:

$$J_{\text{comp}}^{s/d} = J_{\text{max}}^{s/d} \cdot \exp\left(-\frac{(y - y_{\text{max}})^2}{\tau_{s/d}^2}\right) + J_{\text{cen}}^{s/d}, \quad (19)$$

with the maximum B2B tunneling current density value  $J_{\text{max}}^{s/d} = (J_{\text{sur}}^{s/d} - J_{\text{cen}}^{s/d})$  at the position  $y_{\text{max}} = y_{\text{sur}}$ . The parameter  $\tau_{s/d}^2$  is the variance of the Gaussian distribution and is used as an adjustable parameter.

#### E. Tunneling Current

The final step of the compact modeling approach leads to the device B2B tunneling current. Using Eq. (19) and the DG TFET symmetry, means a multiplication by two, the B2B tunneling current is as follows [8]:

$$\begin{aligned} I_{\text{ds}} &= 2 \cdot w_{\text{ch}} \cdot \int_0^{t_{\text{ch}}/2} (J_{\text{comp}}^s(y) + J_{\text{comp}}^d) dy + I_{\text{OFF, TAT}} \quad (20) \\ &= 2 \cdot w_{\text{ch}} \cdot \left\{ \left[ \frac{\sqrt{\pi} \cdot \tau_s \cdot J_{\text{max}}^s}{2} \cdot \text{erf}\left(\frac{y - y_{\text{max}}}{\tau_s}\right) + J_{\text{cen}}^s \cdot y \right] \Big|_0^{t_{\text{ch}}/2} \right. \\ &\quad \left. + \left[ \frac{\sqrt{\pi} \cdot \tau_d \cdot J_{\text{max}}^d}{2} \cdot \text{erf}\left(\frac{y - y_{\text{max}}}{\tau_d}\right) + J_{\text{cen}}^d \cdot y \right] \Big|_0^{t_{\text{ch}}/2} \right\} + I_{\text{OFF, TAT}}. \end{aligned}$$

The term *erf* describes the error function and  $I_{\text{OFF, TAT}}$  characterizes the non-ideal trap-assisted tunneling (TAT) current, which is modeled as a constant in a first assumption.

It should be mentioned, that the presented compact model including approximations of the potential  $\varphi$ , band diagram  $E_{c/v}$  and tunneling length  $l_{\text{tun}}$  are used as an example. That is to say, the presented modeling approach to calculate the closed-form tunneling probability  $T_{\text{tun}}$  in section III is not limited to the presented expressions (see Eqs. (1)–(14)).

### III. AREA-EQUIVALENT WKB APPROACH

In the subsequent section the modeling approach to calculate the B2B tunneling probability  $T_{\text{tun}}$  based on an AE Wentzel-Kramers-Brillouin approximation is introduced for both ON- and AMBIPOLAR-state of the TFET. The general equation to calculate  $T_{\text{tun}}$  using the WKB is given by [6]:

$$T_{\text{tun}} \approx \exp\left(-2 \cdot \int_{x_1}^{x_2} \sqrt{\frac{2 \cdot m^*}{\hbar^2} [U(x) - \mathcal{E}] dx}\right), \quad (21)$$

with the effective carrier mass  $m^*$ , the reduced Planck's constant  $\hbar$ , the tunneling barrier shape along the  $x$ -axis  $U(x)$  and the tunneling energy  $\mathcal{E}$ .

The aim of this work is to establish an expression for the tunneling energy barrier shape  $U(x)$  that characterizes the tunneling barrier of the DG TFET in the ON- and AMBIPOLAR-state of the device in an easy and numerically robust way. Furthermore, the expression ( $\propto \sqrt{U(x)}$ ) must be solvable in a closed-form to obtain a compact equation for  $T_{\text{tun}}$ . Fig. 4(a) illustrates a sketch of the band diagram at the source-to-channel junction showing the tunneling barrier at one specific  $x$ -position  $x_t^s$  in the ON-state of the TFET. On the other hand the tunneling barrier at a chosen  $x$ -value  $x_t^d$  in the AMBIPOLAR-state at the drain-to-channel junction is depicted in Fig. 4(b). In both cases the area of the tunneling barrier is highlighted by red solid lines (hatched areas  $A_1^s$  and  $A_1^d$ , respectively).

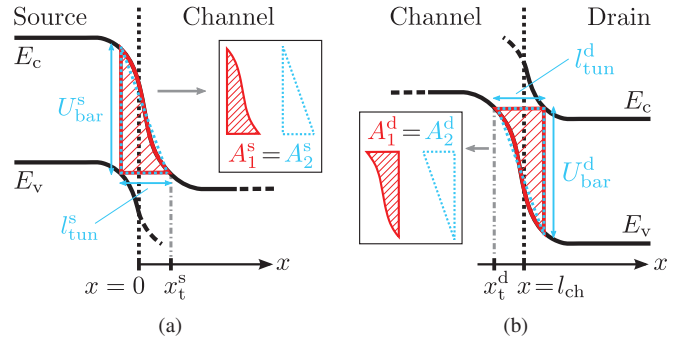


Figure 4. Schematic band diagram at the (a) source-to-channel junction and (b) drain-to-channel junction, showing the shape of the tunneling barrier (red solid lines) at  $x = x_t^{s/d}$  for an arbitrary  $y$ -position. Furthermore, the enclosed area  $A_1^{s/d}$  (red hatched area) as well as the AE triangular (dashed area  $A_2^{s/d}$ ) with its energy barrier height  $U_{\text{bar}}^{s/d}$  and the tunneling length  $l_{\text{tun}}^{s/d}$  are illustrated for both cases.

In literature, a quasi-2D approach for the WKB approximation assuming a triangular energy barrier shape was already published in [9], whereby the calculation of the tunneling barrier height was done using an analytical closed-form 2D electric field solution  $\vec{E}_{2D}$  [17]. The usage of the 2D electric field is very time-consuming and in addition inversion charges are neglected in calculations. Furthermore, the height of the barrier depends only on the result for the electric field in one single point. Therefore, it is very sensitive to any inaccuracies, and hence this model is not appropriate for a robust compact model.

In order to come to a numerically robust implementation, in this work the calculation of the energy barrier height  $U_{\text{bar}}^{s/d}$  is based on an AE approach. In Fig. 4, it can be seen that the area

of the tunneling barrier (hatched area  $A_1^{s/d}$ ) equals the area of a triangle (dashed area  $A_2^{s/d}$ ). Using the area  $A_2^{s/d}$ , an equivalent tunneling barrier height  $U_{\text{bar}}^{s/d}$  for the ON- and AMBIPOLAR-state, respectively, can be obtained after few steps. So in a first step, the area  $A_2^{s/d}$  of the energy triangular is defined by:

$$A_2^{s/d} = \frac{U_{\text{bar}}^{s/d} \cdot l_{\text{tun}}^{s/d}}{2}. \quad (22)$$

By assuming an area equivalence ( $A_1 = A_2$ ), an expression for the area  $A_1$  has to be found. The area  $A_1^s$  of the tunneling barrier in the ON-state is calculated by [18]:

$$A_1^s = \int_{x_t^s - l_{\text{tun}}^s}^{x_t^s} (E_c(x, y) - E_c^{\text{ch},s}(x_t^s, y)) dx \quad (23)$$

$$A_1^s = \int_{x_t^s - l_{\text{tun}}^s}^0 E_c^s(x, y) dx + \int_0^{x_t^s} E_c^{\text{ch},s}(x, y) dx - \int_{x_t^s - l_{\text{tun}}^s}^{x_t^s} E_c^{\text{ch},s}(x_t^s, y) dx,$$

whereby  $E_c^{\text{ch},s}(x_t^s, y)$  defines an offset of the conduction band at the position  $x_t^s$  to obtain the correct area under the curves and to avoid negative area values. Integration by using Eq. (5) and (6) finally leads to:

$$A_1^s = q \cdot \left[ \frac{a_s}{3} \cdot (x_t^s - l_{\text{tun}}^s)^3 + \frac{b_s}{2} \cdot (x_t^s - l_{\text{tun}}^s)^2 + \left( c_s - \frac{E_g^s}{2 \cdot q} \right) \cdot (x_t^s - l_{\text{tun}}^s) + k_s \cdot \ln \left( \frac{l_s}{l_s - x_t^s} \right) + \left( -m_s + \frac{E_g^{\text{ch}}}{2 \cdot q} + \frac{\chi_s - \chi_{\text{ch}}}{q} \right) \cdot x_t^s \right] - E_c^{\text{ch},s}(x_t^s, y) \cdot l_{\text{tun}}^s, \quad (24)$$

whereby the tunneling length  $l_{\text{tun}}^s$  is calculated by Eq. (11).

The AMBIPOLAR-state tunneling barrier area is defined by:

$$A_1^d = \int_{x_t^d}^{x_t^d + l_{\text{tun}}^d} (E_v(x, y) - E_v^{\text{ch},d}(x_t^d, y)) dx \quad (25)$$

$$A_1^d = \int_{x_t^d}^{l_{\text{ch}}} E_v^{\text{ch},d}(x, y) dx + \int_{l_{\text{ch}}}^{x_t^d + l_{\text{tun}}^d} E_v^d(x, y) dx - \int_{x_t^d}^{x_t^d + l_{\text{tun}}^d} E_v^{\text{ch},d}(x_t^d, y) dx.$$

The term  $E_v^{\text{ch},d}(x_t^d, y)$  is used to compensate the valence band offset at the position  $x_t^d$  to obtain the correct tunneling area. With the help of Eq. (9) and (10) the integration is solved as follows:

$$A_1^d = -E_v^{\text{ch},d}(x_t^d, y) \cdot l_{\text{tun}}^d + q \cdot \left[ k_d \cdot \ln \left( \frac{l_d - x_t^d}{l_d - l_{\text{ch}}} \right) + \left( -m_d - \frac{E_g^{\text{ch}}}{2 \cdot q} + \frac{\chi_s - \chi_{\text{ch}}}{q} \right) \cdot (l_{\text{ch}} - x_t^d) + \frac{a_d}{3} \cdot (l_{\text{ch}} - (x_t^d + l_{\text{tun}}^d))^3 + \frac{b_d}{2} \cdot (l_{\text{ch}} - (x_t^d + l_{\text{tun}}^d))^2 - \left( -c_d + \frac{\chi_s - \chi_d}{q} - \frac{E_g^s}{2 \cdot q} \right) \cdot (l_{\text{ch}} - (x_t^d + l_{\text{tun}}^d)) \right], \quad (26)$$

with the tunneling length  $l_{\text{tun}}^d$  for the AMBIPOLAR-state obtained by Eq. (13). It should be noticed that  $A_1^d$  results in a negative value and for this reason the absolute value of  $A_1$  is used in the following.

Using the area of the tunneling barrier  $|A_1^{s/d}| = A_2^{s/d}$  and the tunneling length  $l_{\text{tun}}^{s/d}$  (see Fig. 4), Eq. (22) is rearranged as follows:

$$U_{\text{bar}}^{s/d} = \frac{2 \cdot |A_1^{s/d}|}{l_{\text{tun}}^{s/d}}. \quad (27)$$

In a next step, the energy shape along the  $x$ -axis  $U^{s/d}(x)$  can be characterized by a linear equation as follows:

$$U^{s/d}(x) = -\frac{U_{\text{bar}}^{s/d}}{l_{\text{tun}}^{s/d}} \cdot x + \mathcal{E}^{s/d}. \quad (28)$$

By applying the the expression for  $U^{s/d}(x)$  to the general tunneling probability equation (see Eq. (21)), the tunneling probability for the ON-state is calculated by:

$$T_{\text{tun}}^s = \exp \left( -2 \cdot \int_{x_t^s - l_{\text{tun}}^s}^{x_t^s} \sqrt{\frac{2 \cdot m_s^*}{\hbar^2} \cdot \left( -\frac{U_{\text{bar}}^s}{l_{\text{tun}}^s} \cdot x + \mathcal{E}^s \right) - \mathcal{E}^s} dx \right), \quad (29)$$

which finally leads to the well-known result for the WKB approximation applied to a triangular energy profile:

$$T_{\text{tun}}^s = \exp \left( -\frac{4}{3} \cdot \sqrt{\frac{2 \cdot m_s^*}{\hbar^2} \cdot U_{\text{bar}}^s \cdot l_{\text{tun}}^s} \right). \quad (30)$$

For the AMBIPOLAR-state Eq. (21) is rewritten as:

$$T_{\text{tun}}^d = \exp \left( -2 \cdot \int_{x_t^d}^{x_t^d + l_{\text{tun}}^d} \sqrt{\frac{2 \cdot m_d^*}{\hbar^2} \cdot \left( -\frac{U_{\text{bar}}^d}{l_{\text{tun}}^d} \cdot x + \mathcal{E}^d \right) - \mathcal{E}^d} dx \right) \quad (31)$$

and thus  $T_{\text{tun}}^d$  finally results in:

$$T_{\text{tun}}^d = \exp \left( -\frac{4}{3} \cdot \sqrt{\frac{2 \cdot m_d^*}{\hbar^2} \cdot U_{\text{bar}}^d \cdot l_{\text{tun}}^d} \right). \quad (32)$$

By inserting the expression for  $T_{\text{tun}}^{s/d}$  in Eq. (15), the TGR is calculated to verify the AE modeling approach in the next section.

#### IV. MODELING RESULTS & VERIFICATION

For the verification of the developed AE approach to calculate the tunneling probability in TFETs, the closed-form equations are implemented in an existing TFET compact model [8], [10]. The modeling results are compared to TCAD Sentaurus simulation data of an n-type DG TFET for various simulation setups including hetero-junctions.

Table I contains the default structural parameters, materials, doping concentrations, the applied effective carrier masses as multiples of the electron rest mass  $m_0$  for different materials of the source region and the permittivities of the gate oxide materials. TCAD simulations are performed by including a non-local B2B tunneling model, the model of Slotboom [13] to consider bgn in source and the model of Del Alamo [14]

to take into account bgn in drain. The influence of TAT is simulated with the help of the Hurks TAT model with a maximum trap density  $N_{Tmax}$ . In TCAD the TGR is denoted as *eBarrierTunneling* and *hBarriertunneling* for electrons and holes, respectively [19].

TABLE I  
TCAD SENTAURUS SIMULATION PARAMETER SET FOR SIMULATING THE SHORT-CHANNEL N-TYPE DG TFET.

Parameter	Value	Parameter	Value
$l_{ch}$	22 nm	$t_{ch}$	10 nm
$l_{sd}$	20 nm	$t_{ox}$	2 nm
$w_{ch}$	1 $\mu\text{m}$	$N_s$	$10^{20} \text{ cm}^{-3}$ ( $p^{++}$ )
Drain Material	Silicon	$N_d$	$10^{20} \text{ cm}^{-3}$ ( $n^{++}$ )
Channel Material	Silicon	$N_{Tmax}$	$10^{12} \text{ eV}^{-1} \text{ cm}^{-2}$
Source Material		Effective Carrier Mass	
Silicon	$m_{s,TCAD}^*$	0.26 · $m_0$	
	$m_{d,TCAD}^*$	0.36 · $m_0$	
SiGe	$m_{s,TCAD}^*$	0.18 · $m_0$	
	$m_{d,TCAD}^*$	0.20 · $m_0$	
GaAs	$m_{s,TCAD}^*$	0.059 · $m_0$	
	$m_{d,TCAD}^*$	0.059 · $m_0$	
Germanium	$m_{s,TCAD}^*$	0.15 · $m_0$	
	$m_{d,TCAD}^*$	0.17 · $m_0$	
Gate Oxide Material	Permittivity $\epsilon_{ox}$	Gate Oxide Material	Permittivity $\epsilon_{ox}$
$\text{Y}_2\text{O}_3$	$15 \cdot \epsilon_0$	$\text{La}_2\text{O}_3$	$30 \cdot \epsilon_0$
$\text{HfO}_2$	$22 \cdot \epsilon_0$	$\text{TiO}_2$	$80 \cdot \epsilon_0$
$\text{Ta}_2\text{O}_5$	$26 \cdot \epsilon_0$	—	—

In the first step the modeling results of the electrostatic potential are investigated, since the resulting potential or rather band diagram forms the base of calculations. After that the resulting triangular tunneling barrier is illustrated within the band diagram for various bias conditions and compared with the quasi-2D WKB approach presented in [9]. The third step presents the TGR modeling results in order to verify the resulting tunneling probability. In the last verification step the DC characteristics of the TFET are presented. Here, the compact model is compared to TCAD simulations for various device parameters. In order to do so, the adjustable parameters listed in Table II are applied to the compact model. It should be kept in mind, in this paper it is considered that the source material is silicon and for gate oxide  $\text{HfO}_2$  is chosen except it is mentioned that other materials are used.

#### A. Electrostatic Potential & Band Diagram

The electrostatics of the TFET forms the basis of the calculation of the tunneling probability. Hence, an accurate modeling of the potential and the band diagram is essential for the AE WKB approach. The potential modeling results for the ON-state are illustrated in Fig. 5. In terms of the ON-state the potential and the band diagram are modeled in the

TABLE II  
ADJUSTABLE PARAMETERS OF THE DG TFET COMPACT MODEL FOR VARIOUS SOURCE MATERIALS.

Source Material	Parameter	Value	Parameter	Value
Silicon	$m_s^*$	$0.262 \cdot m_0$	$\tau_s^2$	$1.39 \times 10^{-16} \text{ cm}^2$
	$m_d^*$	$0.28 \cdot m_0$	$\tau_d^2$	$5.0 \times 10^{-17} \text{ cm}^2$
	$\lambda_{fit}^s$	1.25	$\sigma^2$	$5.6 \times 10^{-14} \text{ cm}^2$
	$\lambda_{fit}^d$	1.35	$I_{OFF,TAT}$	$7.0 \times 10^{-16} \text{ A}$
SiGe	$m_s^*$	$0.22 \cdot m_0$	$\tau_s^2$	$4.2 \times 10^{-17} \text{ cm}^2$
	$m_d^*$	$0.26 \cdot m_0$	$\tau_d^2$	$8.0 \times 10^{-17} \text{ cm}^2$
	$\lambda_{fit}^s$	1.30	$\sigma^2$	$5.6 \times 10^{-14} \text{ cm}^2$
	$\lambda_{fit}^d$	1.20	$I_{OFF,TAT}$	$8.0 \times 10^{-16} \text{ A}$
GaAs	$m_s^*$	$0.154 \cdot m_0$	$\tau_s^2$	$3.0 \times 10^{-17} \text{ cm}^2$
	$m_d^*$	$0.24 \cdot m_0$	$\tau_d^2$	$1.9 \times 10^{-16} \text{ cm}^2$
	$\lambda_{fit}^s$	1.25	$\sigma^2$	$5.6 \times 10^{-15} \text{ cm}^2$
	$\lambda_{fit}^d$	1.20	$I_{OFF,TAT}$	$5.0 \times 10^{-16} \text{ A}$
Germanium	$m_s^*$	$0.13 \cdot m_0$	$\tau_s^2$	$4.0 \times 10^{-17} \text{ cm}^2$
	$m_d^*$	$0.28 \cdot m_0$	$\tau_d^2$	$1.7 \times 10^{-16} \text{ cm}^2$
	$\lambda_{fit}^s$	1.20	$\sigma^2$	$5.6 \times 10^{-14} \text{ cm}^2$
	$\lambda_{fit}^d$	1.12	$I_{OFF,TAT}$	$7.0 \times 10^{-15} \text{ A}$

interval  $[-x_1^s \leq x \leq l_{ch}/2]$ . The modeled potential stays in a good agreement compared to TCAD simulations, whereby the small deviations are caused by the chosen fitting parameter to obtain an accurate device current.

In general, the potential is adjustable by the parameters  $\lambda_{fit}^{s/d}$ , which characterizes a fitting parameter to scale the resulting screening length  $\lambda_{s/d}$  at the source-to-channel (ON-state) and drain-to-channel junction (AMBIPOLAR-state). These parameters were introduced in [11].

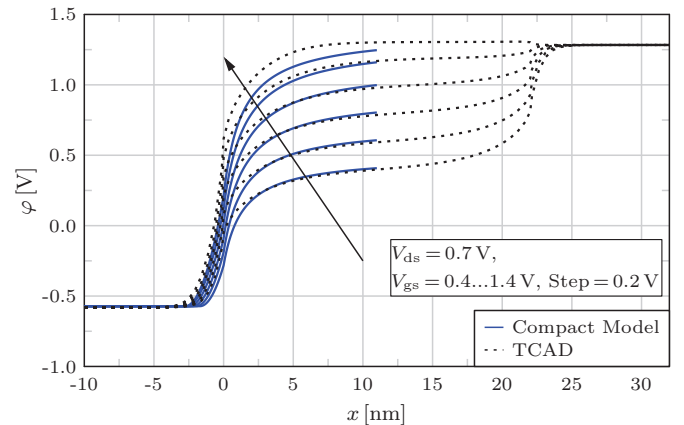


Figure 5. Electrostatic potential of the DG TFET in the ON-state along the  $x$ -axis directly under the gate oxide ( $y = 0 \text{ nm}$ ) for various  $V_{gs}$  values and  $V_{ds} = 0.7 \text{ V}$ . Compact model: Solid lines. TCAD: Dashed lines.

Fig. 6(a) and (b) depict the modeling results for the band diagram at the source-to-channel junction at the channel surface and center in the ON-state. The compact model shows a good fit in comparison with the TCAD data. Furthermore, the influence of bgn can be seen in both modeling and simulation results. The deviations can be explained in the same manner as in the potential.

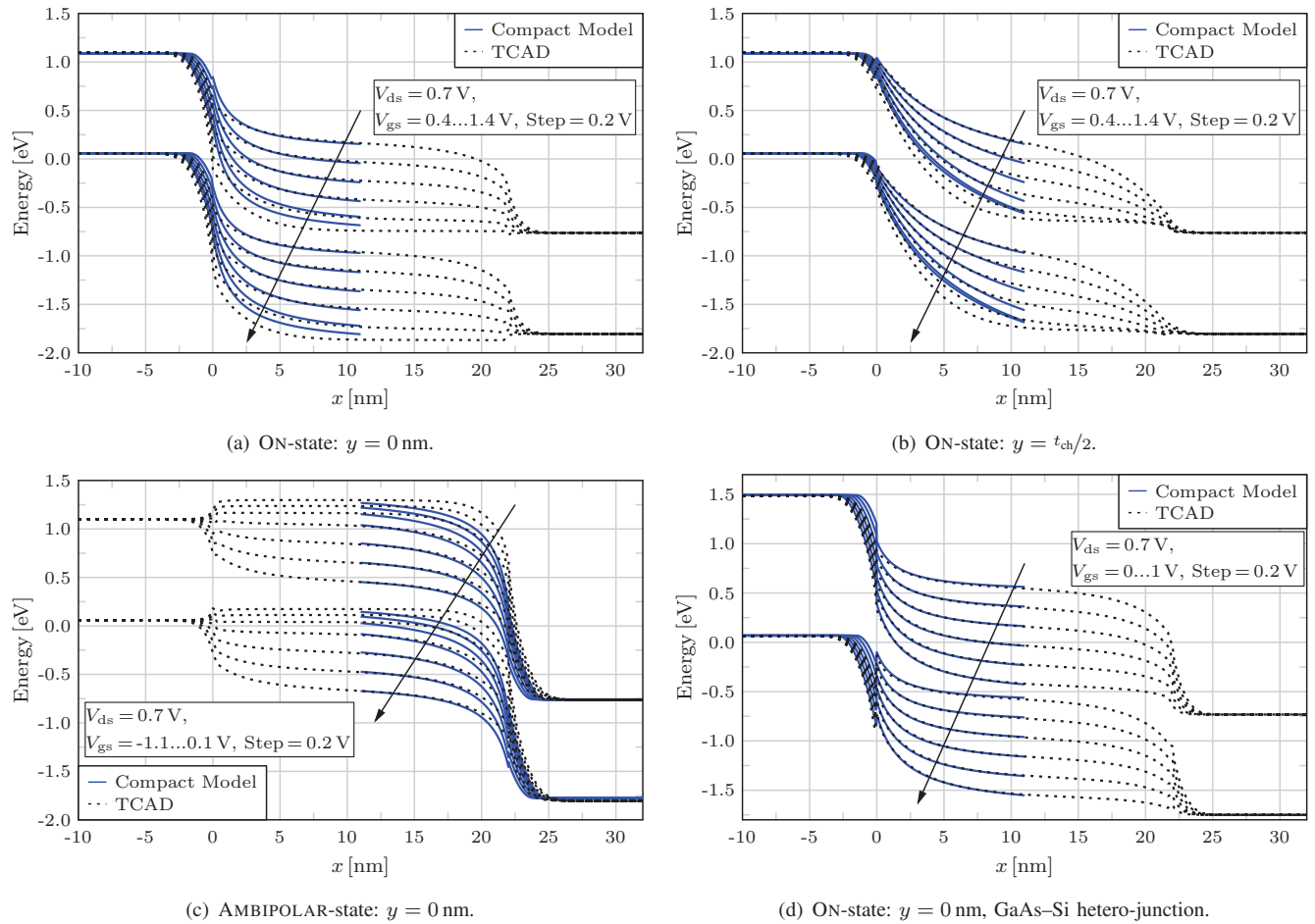


Figure 6. Band diagram of the Silicon DG TFET along the  $x$ -axis and various  $y$ -positions in ON-state (a)-(b) and AMBIPOLAR-state (c) for various gate biases  $V_{gs}$  at  $V_{ds} = 0.7$  V. The GaAs-Si hetero-junction band diagram modeling results are shown in (d). Compact model: Solid lines. TCAD: dashed lines.

The compact modeling results for the AMBIPOLAR-state of the TFET are shown in Fig. 6(c). Since the B2B tunneling in this state occurs mainly at the drain-to-channel junction it is sufficient to characterize the band diagram in the interval  $[l_{ch}/2 < x \leq x_1^d]$ . The results show a good fit compared with the numerical simulation data. The deviations can be explained in the same manner as in the ON-state.

In order to demonstrate the feasibility of simulating hetero-junctions with the compact model, Fig. 6(d) depicts the modeling results of a GaAs-Si DG TFET at the source-to-channel junction. Here the ON-state band diagram is shown to highlight the modeling results at the hetero-junction. It can be seen that the compact model shows a good match compared with the TCAD data.

### B. Tunneling Barrier

With the help of the obtained band diagram of the DG TFET (see Fig. 6(a) - (d)) it is possible to calculate and then visualize the resulting triangular tunneling barrier. In doing so, the compact modeling results of the tunneling barrier height  $U_{bar}^{s/d}$  are compared to the aforementioned quasi-2D WKB approach. In both approaches the tunneling length  $l_{tun}^{s/d}$  is calculated applying Eqs. (11) and (13). The effective carrier masses used in the compact model for various source materials are listed in Table II.

The first results of the tunneling barrier in the ON-state are illustrated in Fig. 7(a) at a drain-source voltage of 0.7 V. In Fig. 7(a)(i), it can be seen that the energy shape  $U^s(x)$  has a similar pattern in comparison to the real barrier defined by the band diagram at a chosen gate bias of  $V_{gs} = 0.9$  V. At this bias point the quasi-2D WKB approach shows a similar shape, where the barrier height  $U_{bar}^s$  is underestimated. An underestimated value for  $U_{bar}^s$  results generally in an overestimation of  $T_{tun}$ . At a gate bias of 1.5 V (see Fig. 7(a)(ii)), the compact model also reproduces the tunneling barrier, whereby the quasi-2D approach leads to an overestimated barrier height. Actually an overestimation of  $U_{bar}$  leads to an underestimated value for the tunneling probability.

Fig. 7(b) illustrates the tunneling barrier in the center of the channel at the same bias conditions as in Fig. 7(a). It can be seen, that the compact model replicates the barrier shape in the center very well, whereby  $U_{bar}^s$  is underestimated in the quasi-2D WKB approach caused by the applied 2D electric field solution. The electric field shows bigger inaccuracies in the channel center than at the surface and hence, the  $U_{bar}$  shows also deviations from the real tunneling barrier height.

In Fig. 7(c)(i), the modeled tunneling barrier in the ON-state does not fit with the tunneling barrier, formed by the band diagram, in both cases. This is a result of the small overlapping area of the valence band in source with the conduction band in the channel.

Here, the advantage of the compact model in comparing with the quasi-2D WKB approach can be pointed out and explained. Using the 2D WKB and assuming an electric field  $|\bar{E}_{2D}| \approx 0 \text{ V/cm}$  leads to a barrier height  $U_{\text{bar}} = 0 \text{ eV}$  and hence to a wrong tunneling probability of  $T_{\text{tun}} = 1$ . By applying the compact model, there is no need to use the electric field and therefore a numerically robust calculation of  $T_{\text{tun}}$  can be achieved. Fig. 7(c)(ii) demonstrates the modeling results for a smaller  $V_{\text{ds}} = 0.1 \text{ V}$  and  $V_{\text{ds}} = 1.5 \text{ V}$ . It can be seen that the tunneling barrier is reproduced well by both models.

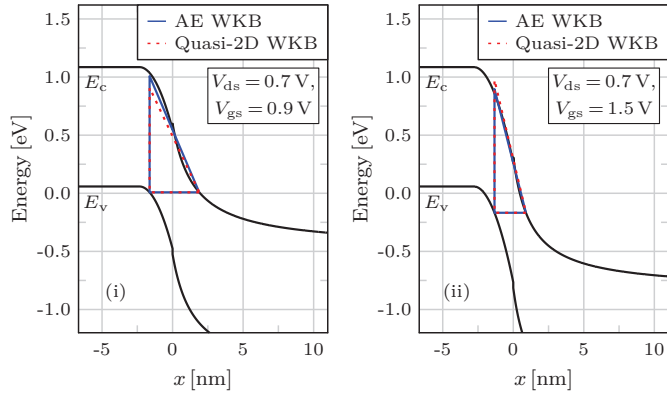
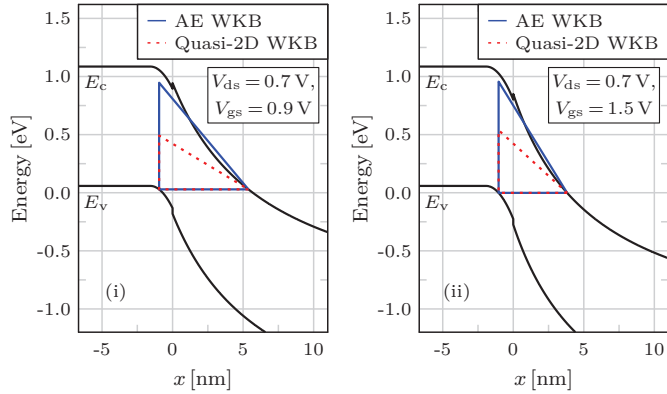
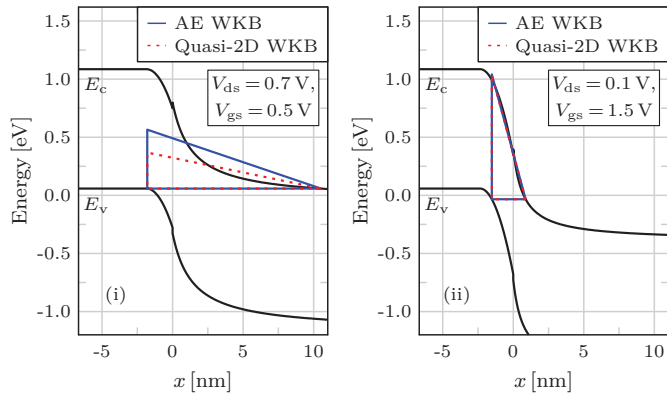
(a) ON-state:  $y = 0 \text{ nm}$ .(b) ON-state:  $y = t_{\text{ch}}/2$ .(c) ON-state:  $y = 0 \text{ nm}$ .

Figure 7. ON-state modeling results of the tunneling barrier illustrated in the band diagram at the surface in (a) & (c) and in the center of the channel in (b). The AE WKB approach (triangle with blue solid lines) is compared to the quasi-2D WKB approach (triangle with red dashed lines).

Figures 8(a) and (b) show the resulting tunneling barrier  $U^{\text{d}}(x)$  in the AMBIPOLAR-state, located at the drain-to-channel junction, for  $y = 0 \text{ nm}$  and  $y = t_{\text{ch}}/2$  at gate bias of  $V_{\text{gs}} = -1.2 \text{ V}$  and  $V_{\text{gs}} = -0.1 \text{ V}$ , respectively. In the four plots the AE WKB approach reproduces the tunneling barrier height  $U_{\text{bar}}^{\text{d}}$  in a good way, whereby the quasi-2D WKB approach shows the same deviations as in the ON-state shown in Fig. 7(a) and 7(b).

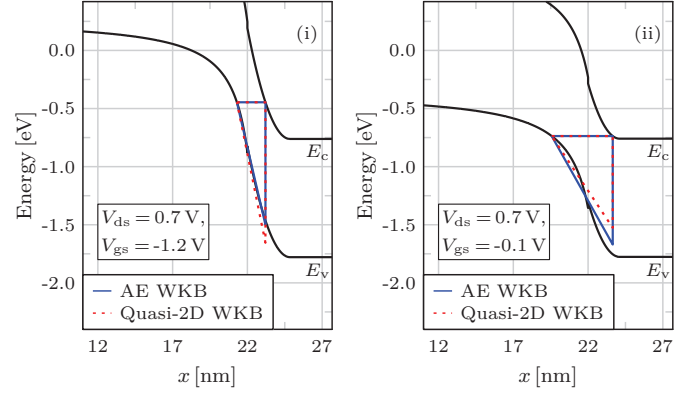
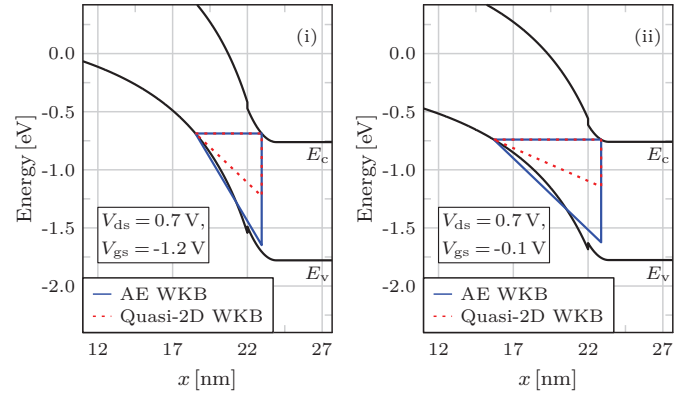
(a) AMBIPOLAR-state:  $y = 0 \text{ nm}$ .(b) AMBIPOLAR-state:  $y = t_{\text{ch}}/2$ .

Figure 8. Resulting tunneling barrier in the AMBIPOLAR-state at (a) the surface and in (b) the center of the channel for  $V_{\text{gs}} = -1.2 \text{ V}$  and  $V_{\text{gs}} = -0.1 \text{ V}$  at  $V_{\text{ds}} = 0.7 \text{ V}$ , respectively. AE WKB: Solid blue triangle. Quasi-2D WKB: Dashed red triangle.

In order to demonstrate the ability of simulating heterojunctions, figures 9(a) and (b) depict the modeled tunneling barrier height  $U_{\text{bar}}^{\text{s}}$  in the ON-state for a GaAs-Si heterojunction. In this case the effective carrier masses  $m_{\text{s/d}}^*$  need to be adapted (see Table II). In Fig. 9(a)(i), the AE WKB approach underestimates the tunneling barrier height in the transition from the OFF- to the ON-state by assuming a fitting to obtain a correct device current. The quasi-2D approach results only in half value of  $U_{\text{bar}}^{\text{s}}$  which is again a consequence of the used electric field solution. Fig. 9(a)(ii) demonstrates the ON-state ( $V_{\text{gs}} = 1.2 \text{ V}$ ) of the hetero-junction TFET. As it can be seen the AE WKB approach predicts the tunneling barrier well, whereby the quasi-2D approach underestimates  $U_{\text{bar}}^{\text{s}}$ . The results in the center of the channel are illustrated in Fig. 9(b), at both gate biases the tunneling barrier height is predicted well. The barrier heights calculated by the quasi-2D approach are incorrect due to the applied electric field solution.

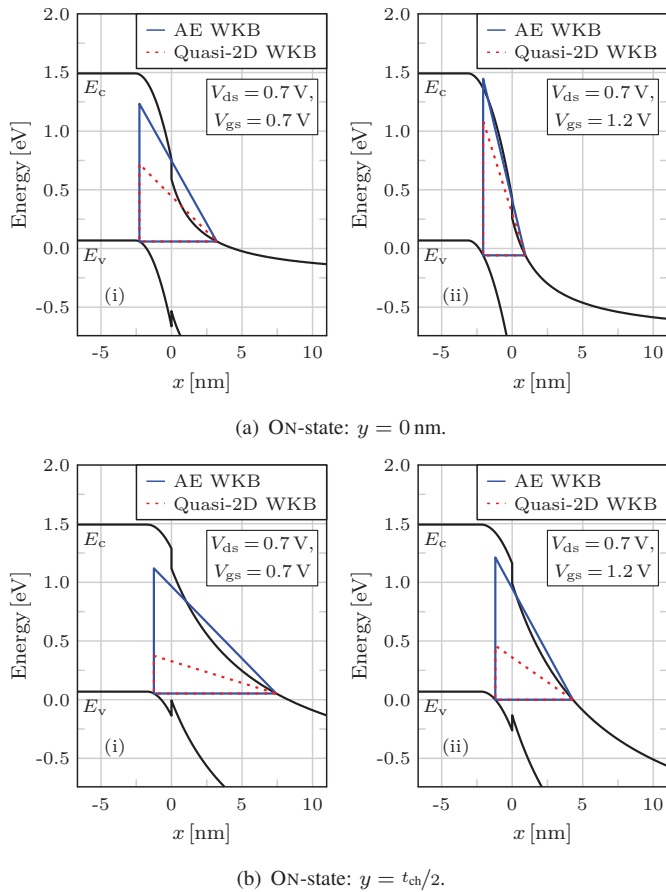


Figure 9. GaAs-Si hetero-junction tunneling barrier modeling results, located at the source-to-channel junction, in the ON-state at (a) the surface and in (b) the center of the channel. Bias:  $V_{gs} = 0.7$  V and  $V_{gs} = 1.2$  V at  $V_{ds} = 0.7$  V. AE WKB: Solid blue triangle. Quasi-2D WKB: Dashed red triangle.

### C. Tunneling Generation Rate

The verification of the AE WKB by TCAD simulations is done in terms of the TGR since TCAD cannot display the transmission coefficient along the  $x$ -axis. To do so, the TGR is calculated for various  $y$ -positions in the channel with the help of Eq. (15) and compared to TCAD data. All verification steps are performed for different gate-source voltages  $V_{gs}$  at  $V_{ds} = 0.7$  V.

Fig. 10(a) presents the resulting TGR at the surface of a Silicon DG TFET in ON-state. In this figure the TGR calculated by the compact model is compared to TCAD simulations and also to the TGR obtained by using the quasi-2D WKB approach. The compact modeled TGR shows a horizontal displacement along the  $x$ -axis in contrast to TCAD, which is caused by the chosen adjustable parameters  $\lambda_{fit}^{s/d}$  for a correct  $I_{ds}$ . But the amount and shape of the compact TGR result in the same pattern. This horizontal offset has little influence on the resulting current density along the  $y$ -axis, which is obtained by integration of Eq. (15). The TGR calculated with the quasi-2D WKB approach overestimates the amount of the TGR at all gate biases  $V_{gs}$  which as a consequence leads to an overestimation of the resulting device current. For this reason, the occurring deviation must be scaled down by an additional fitting parameter which is avoided by the new AE compact model approach.

The modeling results in the channel center are depicted in Fig. 10(b) for the same applied voltages. The results of the modeled TGR show an underestimation for the chosen  $V_{gs}$  range in comparison with TCAD data. This is to explain by the selected adjustable fitting parameter to obtain a correct device current. In Fig. 6(b) one can see small deviations in the modeled band diagram, which causes an overestimated tunneling length  $l_{tun}^s$  and hence an underestimated value for  $T_{tun}^s$  ( $\propto \exp(-l_{tun}^s)$ ). Nevertheless, the center TGR is four orders of magnitude smaller than the surface TGR and thus the contribution to the device B2B tunneling current is small. Hence, the deviations in the center TGR are tolerable. The results of the TGR using the quasi-2D approach are omitted in Fig. 10(b) since the obtained TGR values are two orders of magnitude higher than TCAD data, which again demonstrates the inaccuracies of the electric field in the center of the channel.

In Fig. 10(c) the TGR at the channel surface in the AMBIPOLAR-state is shown for various  $V_{gs}$  values. As it is also recognizable in Fig. 10(a), a horizontal offset occurs in the AMBIPOLAR-state caused by the chosen fitting parameters listed in Table II. The amount and shape of the TGR show a good agreement with TCAD simulations so that an integration along the  $x$ -axis results in a correct current density.

Fig. 10(d) illustrates the TGR modeling results at the surface of a GaAs-Si hetero-junction DG TFET in the ON-state. As it can be seen the amount and shape of the compact TGR shows a very good fit in comparison to the numerical TCAD simulations. The occurring  $x$ -offset is to explain in the same manner as in the aforementioned paragraphs.

### D. Tunneling Current

The verification of the B2B tunneling current for various bias conditions and device parameters is used to demonstrate the numerical robustness and flexibility of the AE WKB approach and as well as the compact TFET model.

At first, the transfer characteristic for various drain-source voltages  $V_{ds}$  is under investigation. Fig. 11(a) presents the modeling results in comparison to TCAD simulation data. The compact model stays in good agreement with the numerical data in logarithmic and even in linear scale. An increasing drain-source voltage does not influence the ON-state subthreshold slope and the threshold voltage, respectively, since B2B tunneling occurs at the source-to-channel junction and this junction is not influenced by  $V_{ds}$ . For a small  $V_{ds} = 0.1$  V the effect of inversion charges becomes visible for  $V_{gs} \geq 0.8$  V, which results in a saturation of the current. This effect can also lightly be seen for  $V_{ds} = 0.3$  V. In the AMBIPOLAR-state the increase of  $V_{ds}$  causes a shift to the right along the  $V_{gs}$ -axis, hence the AMBIPOLAR threshold voltage is also shifted to more positive values. This effect is caused by the B2B tunneling occurring at the drain-to-channel junction, which is affected by drain-source voltage.

In Fig. 11(b) the transfer curves for different materials of the source region at  $V_{ds} = 0.7$  V are depicted. By modifying the source material the behavior of the B2B tunneling process at the source-to-channel junction is also changed. The changes in the physical parameters like band gap, electron affinity,

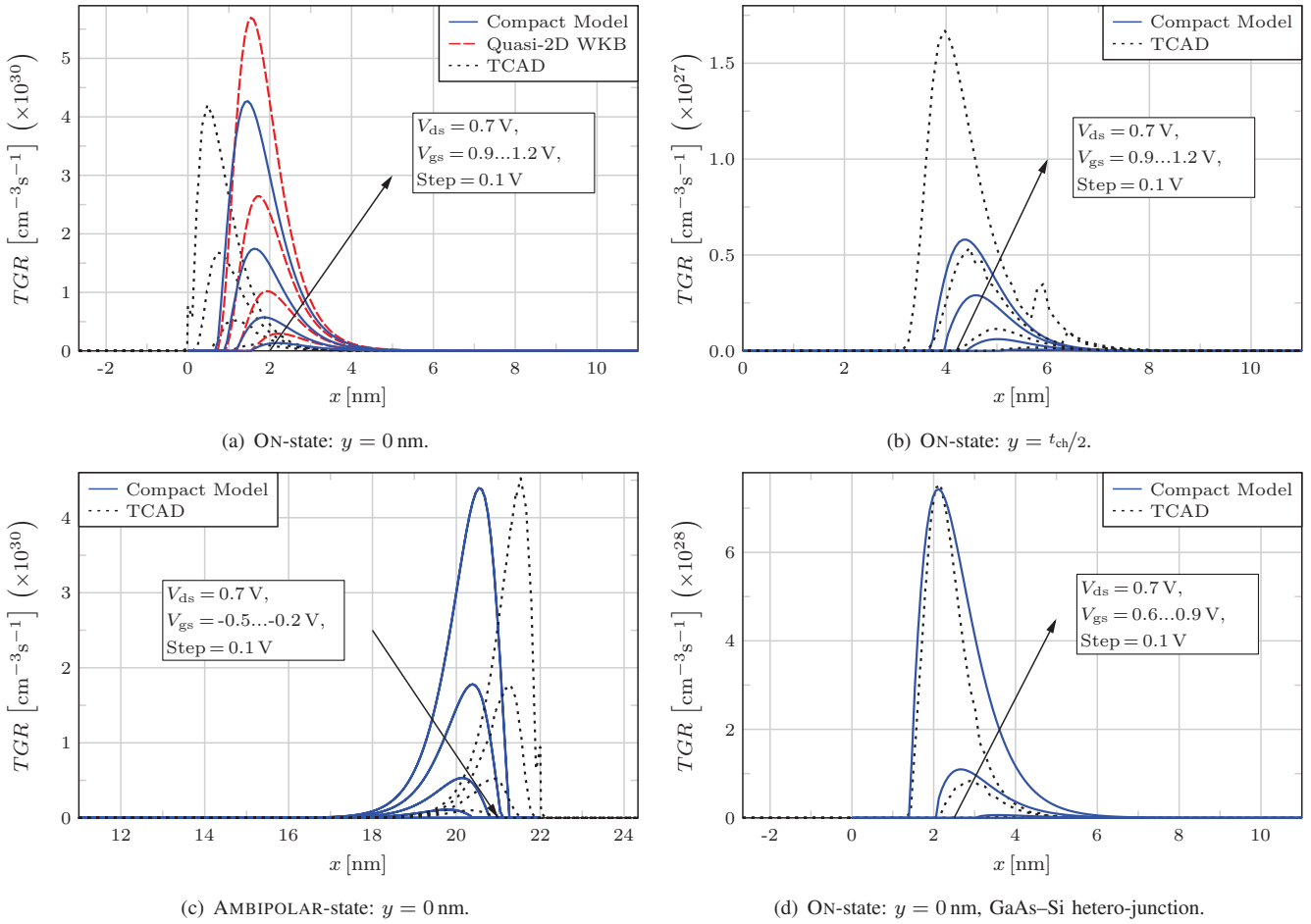


Figure 10. TGR compact modeling results of the Silicon DG TFET along the  $x$ -axis and different  $y$ -positions in the ON-state (a)-(b) and the AMBIPOLAR-state (c) for several  $V_{gs}$  and  $V_{ds} = 0.7$  V. In (a), the TGR calculated using the quasi-2D WKB is also shown and compared to the compact model and TCAD data. TGR results of the GaAs-Si hetero-junction in the ON-state are illustrated in (d). Compact model: Solid lines. Quasi-2D WKB: Coarse dashed lines. TCAD: Fine dashed lines.

permittivity and effective carrier masses have an impact on the resulting subthreshold slope, maximum ON-current and threshold voltage. In case of SiGe ( $E_g^{SiGe} = 0.78$  eV,  $\epsilon_{SiGe} = 13.95 \cdot \epsilon_0$ ,  $\chi_{SiGe} = 4.036$  eV), the maximum ON-state current is increased by a factor 4.4 at  $V_{gs} = 1.2$  V. The subthreshold slope at  $V_{gs} = 0.55$  V results in  $S_{th}^{SiGe} = 19.1$  mV/dec, which is steeper than in the Si device  $S_{th}^{Si} = 23.0$  mV/dec. The OFF-state current is in the same order of magnitude in comparison to Silicon. These enhancements are due to the smaller band gap and the lower effective electron mass. For the source material GaAs,  $E_g^{GaAs} = 1.422$  eV,  $\epsilon_{GaAs} = 13.18 \cdot \epsilon_0$ ,  $\chi_{GaAs} = 4.07$  eV, the maximum ON-state current at  $V_{gs} = 1.2$  V decreases by the factor 9.7 and the slope worsens to  $S_{th}^{GaAs} = 31.7$  mV/dec in comparison to the Si device. This degradation is to explain by the bigger band gap of GaAs even though it has a smaller effective electron mass than Silicon. The last investigated source material is Germanium having the physical parameters  $E_g^{Ge} = 0.6638$  eV,  $\epsilon_{Ge} = 15.8 \cdot \epsilon_0$ ,  $\chi_{Ge} = 4.00$  eV. Germanium with its small band gap and effective electron mass causes a subthreshold slope of  $S_{th}^{Ge} = 19.9$  mV/dec at  $V_{gs} = 0.51$  V and a maximum ON-state current at  $V_{gs} = 1.2$  V which is 30 times higher in comparison to the Si TFET. Unfortunately, the OFF-state current also increases by one order of magnitude, which shrinks the resulting ON/OFF-ratio. The compact model fits

very well in linear and logarithmic scale for all chosen source materials compared to TCAD data.

Figures 11(c) - (f) present the modeling results for varying device parameters in comparison to TCAD simulations. All results of the parameter variation are simulated at a drain-source-voltage of 0.7 V, whereby the adjustable parameters in Table II stay constant and are not changed in this analysis. In Fig. 11(c) the channel length of the TFET is varied from  $l_{ch} = 22 - 65$  nm. The results of the compact model show a good match in comparison to TCAD data. An increasing channel length opens the possibility of more carriers generated in the channel and for this reason the resulting B2B device current increases with increasing  $l_{ch}$ .

Next, the channel thickness is varied in the range  $t_{ch} = 8 \dots 15$  nm (see Fig. 11(d)). The compact model is able to predict the change in  $t_{ch}$  in a good way. The occurring deviations in the transfer curve in contrast to TCAD simulations can easily be reduced with the parameters  $\tau_s^2$  and  $\tau_d^2$  that characterize the current density along the  $y$ -axis.

A variation of the of the gate oxide thickness in the range of  $t_{ox} = 1.5 \dots 2.5$  nm is illustrated in Fig. 11(e), thereby the compact model is compared to TCAD simulation results and shows a good agreement. The influence of the gate oxide thickness on the electrostatics and as a consequence on the

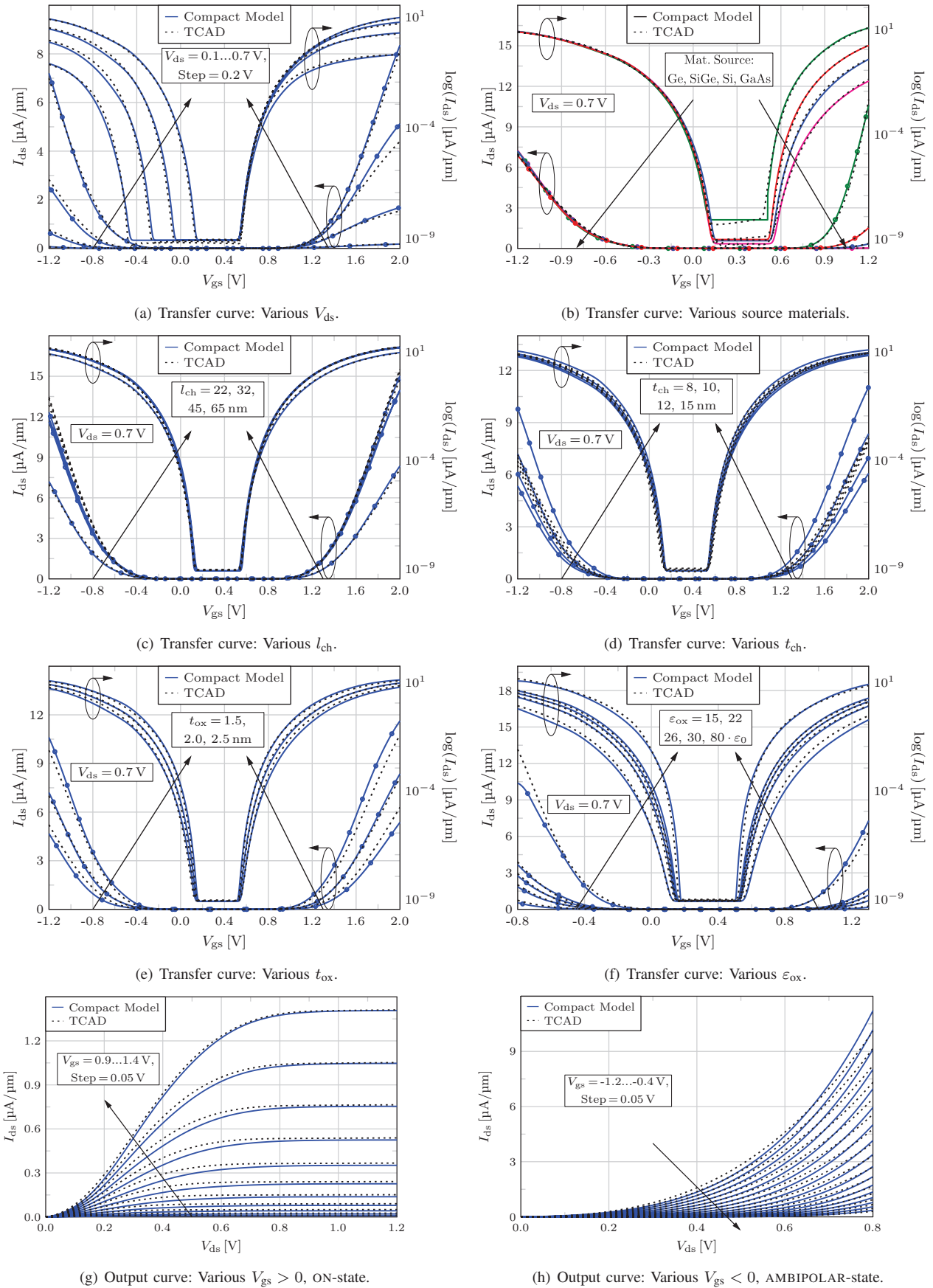


Figure 11. Current characteristics of the DG TFET. Compact modeling results (solid lines) are compared to TCAD Sentaurus simulation data (dashed lines). (a)-(f): Transfer curves for various sets of device parameters like source material, device dimensions and bias conditions. (g)-(h): Output curves for the ON- and AMBIPOLAR-state of the device.

device current can be seen in this plot. A smaller  $t_{ox}$  opens the possibility of a better electrostatic control of the channel region, means a steeper tunneling junction and hence a higher  $I_{ds}$ . For thicker  $t_{ox}$  it is vice versa.

Similar to the change in  $t_{ox}$ , the gate oxide material and so the permittivity of the gate oxide  $\epsilon_{ox}$  can be varied to control the electrostatic influence on the channel region. The simulated gate oxide materials and its related  $\epsilon_{ox}$  values are listed in Table I. Fig. 11(f) shows the compact model transfer curve for various  $\epsilon_{ox}$  values in comparison to TCAD simulations. The compact model fits well for the simulated gate oxide materials  $\epsilon_{ox} = 15 \dots 80 \cdot \epsilon_0$ , whereby a higher permittivity causes a better electrostatic control of the channel and thus a higher device current. The small deviations occurring for  $\epsilon_{ox} = 15 \cdot \epsilon_0$  are due to the adapted fitting parameters (see Table II) which are chosen to be constant.

The compact model results of the output characteristics are shown in Fig. 11(g) and (h). The ON-state output curve is depicted in Fig. 11(g). The compact model stays in good agreement with the TCAD simulation for various gate biases  $V_{gs}$ , even the exponential increase of  $I_{ds} \propto T_{tun}$  for small  $V_{ds}$  is predicted very well. For higher  $V_{ds}$  values, depending on the chosen gate bias, the B2B tunneling current saturates.

Due to the AMBIPOLAR behavior of the TFET, there also exists an output curve for negative  $V_{gs}$ , which is shown in Fig. 11(h). The compact model shows a good agreement with the TCAD data. The curves show an exponential increase of the current in the applied drain-voltage range. The reason for that is the tunneling process occurring at the drain-to-channel junction, whereby the tunneling barrier is only determined by the drain-source voltage at a fixed  $V_{gs}$ . The effect of inversion charges does not play a role in this operating area of the TFET.

## V. CONCLUSION

This paper introduced a novel analytical concept to predict the tunneling probability in TFETs based on an area equivalence of the real and the simplified triangular tunneling energy barrier used in the WKB approximation. The approach can easily be implemented in TFET compact models, where the model must provide compact equations for the band diagram and the tunneling length. An existing compact TFET model was used to demonstrate the practicability and verification of the AE approach.

Verification was done by performing numerical TCAD simulations of a DG TFET including hetero-junctions and device parameter variation. The comparison of the compact modeling results to TCAD data offered a good match for the device band diagram, tunneling generation rate and B2B tunneling current in ON- and AMBIPOLAR-state. The illustration and validation of the triangular tunneling barrier was done within the band diagram results of the compact model, thereby the AE WKB approach was compared to a quasi-2D WKB approach. The comparison showed the higher accuracy of the novel approach, e.g. in the TGR, with simultaneous reduction of complexity.

Numerical stability and robustness as well as model flexibility were shown in the modeling results which opens up the possibility of a universal usage of the AE WKB approach in general TFET compact models.

## ACKNOWLEDGMENT

We would like to thank Keysight Technologies for the license donation and support of the software IC-CAP and AdMOS GmbH for support.

## REFERENCES

- [1] B. Razavi, *Design of Analog CMOS Integrated Circuits*. New York, NY 10020, USA: Tata McGraw-Hill, 2001.
- [2] D. J. Frank, R. H. Dennard, E. Nowak, P. M. Solomon, Y. Taur, and H.-S. P. Wong, "Device scaling limits of Si MOSFETs and their application dependencies," *Proceedings of the IEEE*, vol. 89, no. 3, pp. 259–288, Mar. 2001.
- [3] A. C. Seabaugh and Q. Zhang, "Low-voltage tunnel transistors for beyond CMOS logic," *Proceedings of the IEEE*, vol. 98, no. 12, pp. 2095–2110, Dec. 2010.
- [4] H. Lu and A. Seabaugh, "Tunnel field-effect transistors: State-of-the-art," *IEEE Journal of the Electron Devices Society*, vol. 2, no. 4, pp. 44–49, Jul. 2014.
- [5] A. M. Ionescu and H. Riel, "Tunnel field-effect transistors as energy-efficient electronic switches," *Nature*, vol. 479, no. 7373, pp. 329–337, Nov. 2011.
- [6] S. M. Sze and K. K. Ng, *Physics of semiconductor devices*, 3rd ed. Hoboken, New Jersey, USA: John Wiley & Sons, Inc., 2007.
- [7] A. Gehring, "Simulation of tunneling in semiconductor devices," Ph.D. dissertation, Technische Universität Wien, Austria, 2003.
- [8] F. Horst, A. Farokhnejad, Q. Zhao, B. Iñíguez, and A. Kloes, "2-D physics-based compact DC modeling of double-gate tunnel-FETs," *IEEE Transactions on Electron Devices*, pp. 1–7, Jul. 2018.
- [9] M. Graef, T. Holtij, F. Hain, A. Kloes, and B. Iñíguez, "A 2D closed form model for the electrostatics in hetero-junction double-gate tunnel-FETs for calculation of band-to-band tunneling current," *Microelectronics Journal*, vol. 45, no. 9, pp. 1144–1153, Sep. 2014.
- [10] F. Horst, M. Graef, F. Hosenfeld, A. Farokhnejad, F. Hain, G. V. Luong, Q.-T. Zhao, B. Iñíguez, and A. Kloes, "Implementation of a DC compact model for double-gate Tunnel-FET based on 2D calculations and application in circuit simulation," in *2016 46th European Solid-State Device Research Conference (ESSDERC)*. IEEE, Sep. 2016, pp. 456–459.
- [11] M. Graef, T. Holtij, F. Hain, A. Kloes, and B. Iñíguez, "Improved analytical potential modeling in double-gate tunnel-FETs," in *2014 Proceedings of the 21st International Conference Mixed Design of Integrated Circuits and Systems (MIXDES)*. IEEE, Jun. 2014, pp. 49–53.
- [12] L. Zhang and M. Chan, "SPICE modeling of double-gate tunnel-FETs including channel transports," *IEEE Transactions on Electron Devices*, vol. 61, no. 2, pp. 300–307, Feb. 2014.
- [13] J. Slotboom and H. De Graaff, "Measurements of bandgap narrowing in Si bipolar transistors," *Solid-State Electronics*, vol. 19, no. 10, pp. 857–862, Oct. 1976.
- [14] J. del Alamo, S. Swirhun, and R. M. Swanson, "Simultaneous measurement of hole lifetime, hole mobility and bandgap narrowing in heavily doped n-type silicon," in *1985 International Electron Devices Meeting*. IEEE, Dec. 1985, pp. 290–293.
- [15] R. Tsu and L. Esaki, "Tunneling in a finite superlattice," *Appl. Phys. Lett.*, vol. 22, no. 11, pp. 562–564, Jun. 1973.
- [16] C. B. Duke, *Tunneling in solids*. Academic Press, 1969, vol. 10.
- [17] M. Schwarz, T. Holtij, A. Kloes, and B. Iñíguez, "Complex 2D electric field solution in undoped double-gate MOSFETs," *IETE Journal of Research*, vol. 58, no. 3, pp. 197–204, Sep. 2012.
- [18] F. Horst, A. Parokhnejad, B. Iñíguez, and A. Kloes, "An area equivalent WKB approach to calculate the b2b tunneling probability for a numerical robust implementation in TFET compact models," in *2018 25th International Conference "Mixed Design of Integrated Circuits and System" (MIXDES)*. IEEE, Jun. 2018, pp. 45–50.
- [19] Synopsys Inc., *TCAD Sentaurus Device User Guide*, 2012, Version G-2012.06.



**Fabian Horst** received the M.Sc. degree in electronic engineering from the TH Mittelhessen University of Applied Sciences (THM), Giessen, Germany, in 2015. He is currently pursuing the Ph.D. degree with University Rovira i Virgili, Tarragona, Spain, in cooperation with THM.



**Benjamín Iñíguez** received the B.S., M.S., and Ph.D. degrees in physics from the University of the Balearic Islands, Palma, Spain, in 1989, 1992, and 1996, respectively.

Since 2010, he has been a Full Professor with the Department of Electrical Electronic Engineering and Automation, Universitat Rovira i Virgili, Tarragona, Spain. His current research interests are compact modeling of advanced electronic devices, parameter extraction, and electrical characterization.



**Atieh Farokhnejad** received the M.Sc. degree in information and communication engineering from TH Mittelhessen University of Applied Sciences (THM), Giessen, Germany, in 2015. She is currently pursuing the Ph.D. degree with University Rovira i Virgili, Tarragona, Spain, in cooperation with THM.



**Alexander Kloes** received the Diploma and Ph.D. degrees in electrical engineering from the Solid-State Electronics Laboratory, Technical University of Darmstadt, Darmstadt, Germany, in 1993 and 1996, respectively.

Since 2002, he has been a Professor with the TH Mittelhessen University of Applied Sciences, Giessen, Germany. His current research interests include modeling of semiconductor devices, especially for nanoscale MOS devices and organic TFTs.



**Ghader Darbandy** received the Master and Ph.D. degrees in electrical engineering from the University of Rovira i Virgili, Tarragona, Spain, in 2009 and 2012, respectively. He has been a Research Associate at the Competence Center for Nanotechnology and Photonics, THM, Giessen, Germany since 2018.

From 2013 to 2018, he was a Postdoctoral Fellow at the Department of Electrical Engineering and the Center for Advancing Electronics Dresden (cfaed), TU-Dresden, Dresden, Germany.